JOURNAL OF AIRCRAFT
Vol. 46, No. 1, January–February 2009

Novel Algorithm for Simulating the General Parachute-Payload System: Theory and Validation

Peng Ke* and Chunxin Yang†
Beihang University, 100083 Beijing, People's Republic of China
and
Xiaowei Sun‡ and Xuesong Yang‡
Aerospace Life-Support Industries, Ltd., 441022 Hubei, People's Republic of China

DOI: 10.2514/1.34240

A novel algorithm to model and simulate the general parachute-payload system was developed. This algorithm adopted the multibody system method and the Kane equation to analyze dynamically the parachute-payload system. Two main aspects of the algorithm were discussed: treating the parachute system as a special multibody system and establishing universal methods to select the general coordinates. The chosen general coordinates were suitable for the parachute-payload system to describe the kinematics of the system. The Kane equation and its augmented form aiming at systems with variable mass were applied to create kinetic equations. Additionally, some special issues in simulating the parachute-payload system, such as parachute opening and contacting between the parachute cluster and the sling system, were further analyzed within a unified framework. A solver to numerically implement the proposed algorithm was developed by using C++. The solver was able to read the formatted configuration files of a concrete parachute system and to uniformly conduct the simulation for the different stages during the entire airdrop process. The algorithm and solver were verified by some examples obtained from literature or generated by commercial software and were applied successfully to investigating many kinds of parachute-payload systems.

Nomenclature

$\boldsymbol{C}, \boldsymbol{D}, \boldsymbol{E}$	=	auxiliary matrices
$\tilde{\boldsymbol{e}}$	=	local derivative of the rotation reference
$\boldsymbol{F}, \boldsymbol{M}$	=	force and torque
$\boldsymbol{H}_{i,j}$	=	transform matrix from reference frame j to reference frame i
$\boldsymbol{H}^H_{b,h}$	=	map matrix for linear velocity
$\boldsymbol{H}^h_i$	=	speed transform matrix of body i
$\boldsymbol{H}^\Omega_{b,h}$	=	map matrix for angular velocity
$\boldsymbol{H}^\Omega_i$	=	angular speed transform matrix of body i
$\boldsymbol{J}$	=	inertia tensor
L_i	=	set of bodies in the branch from 0 to the body i
$L^n(i)$	=	nth inside body index of the body i ($n = 0, 1, \ldots$)
$m, \boldsymbol{m}$	=	mass and mass matrix
$\boldsymbol{q}, \dot{\boldsymbol{q}}$	=	vector of the generalized coordinates and their derivative
$\boldsymbol{r}, \boldsymbol{d}$	=	vector of position
$\boldsymbol{S}(\boldsymbol{v})$	=	skew matrix of the vector $\boldsymbol{v}$
$\boldsymbol{T}$	=	channel matrix of the multibody system
$\boldsymbol{V}, \boldsymbol{v}$	=	vector of linear velocity
$\boldsymbol{\alpha}, \boldsymbol{\lambda}$	=	auxiliary matrices
$\boldsymbol{\beta}, \boldsymbol{\sigma}, \boldsymbol{\eta}$	=	auxiliary vectors
$\gamma, \varphi, \vartheta$	=	Euler angle triplet
$\boldsymbol{\Omega}, \boldsymbol{\omega}$	=	vector of angular velocity

Subscripts

i, j	=	body index
r	=	relative

Superscripts

a	=	inertial (force or torque)
o	=	external (force or torque)
T	=	transform of the matrix
$*$	=	generalized inertial (force or torque)

I. Introduction

PARACHUTE systems are being widely used in many fields nowadays, such as spacecraft recovery, planet probe landing, and rapid aerial delivery of equipment and supplies. In a typical heavy-cargo airdrop system (HCADS) [1], the parachute system becomes very complex. The HCADS is composed of 10 parachutes, including one extraction parachute, one pilot parachute, four relatively small drogue parachutes, and four main parachutes. The payload usually weighs more than 7 t. In such a complex parachute-payload system (PPS), parachutes deploy in a prearranged sequence to decelerate the payload in a controlled fashion, resulting in drastic changes in system configuration at different stages of the airdrop process.

The computer simulation technique, which is able to predict the performance of parachute system and provide alternatives to or complements to drop tests as well as laboratory experiments, has significantly enhanced the technology of the airdrop system. However, it still is a challenge to develop a universal approach that is suitable for different parachute system configurations, due to the complexity of the parachute cluster, the payload and sling system, the unavoidable variations in parachute inflation, and the elasticity of all components.

Researchers have dedicated great efforts to build models to simulate different particular configurations. For example, Fallon [2] developed a planar model to analyze the Queen match recovery system, in which a single parachute is connected to a payload through a textile line with a defined elasticity. Moulin [3] discovered the importance of the contribution of the link in the dynamic behavior of the typical parachute system used for planetary entry. In the same study, the author established an 8 DOF (degrees of freedom) model by assigning a certain amount of mass to the confluence point. A

Received 27 February 2008; revision received 9 October 2008; accepted for publication 11 October 2008.

*Postdoctoral Researcher, School of Transportation Science and Engineering; p.ke@buaa.edu.cn. Member AIAA.
†Professor, School of Aeronautical Science and Engineering; yangchunxin@sina.com (Corresponding Author).
‡Senior Engineer.

similar model with the bridle collapse taken into consideration using geometry method was developed by Raiszadeh and Queen [4,5]. As a part of decelerator system simulation, Cuthbert [6], Cuthbert and Desabrais [7], Cuthbert and Conley [8], and Potvin et al. [9] established a 2-dimensional model for the four bridles in the drogue sling system and used riser angle to determine sling configuration by comparing it with the sling angles. Raiszadeh [10] modeled the confluence point as an equilibrium point to overcome the numerical stiffness caused by the little mass point of confluence during simulation. NASA employed their own software (such as POST [5] and DSENDS [11]) for spacecraft simulation to conduct the trajectory analysis of the planetary landing system. Each model mentioned previously was developed for a specific system configuration or stage. It is therefore necessary to develop a universal method to simulate the general parachute system during the entire process.

The primary purpose of this paper is therefore to propose a novel algorithm to model and simulate the general PPS during the entire deployment process. The algorithm, simulating the PPS as a multibody system, will address all complex issues stated previously with the aid of multibody system dynamics [12] and can be applied easily to simulate various types of PPS, such as a cargo airdrop system, planetary entry systems, and personnel parachutes. In particular, the different stages during the entire deployment process of the PPS can be simulated uniformly.

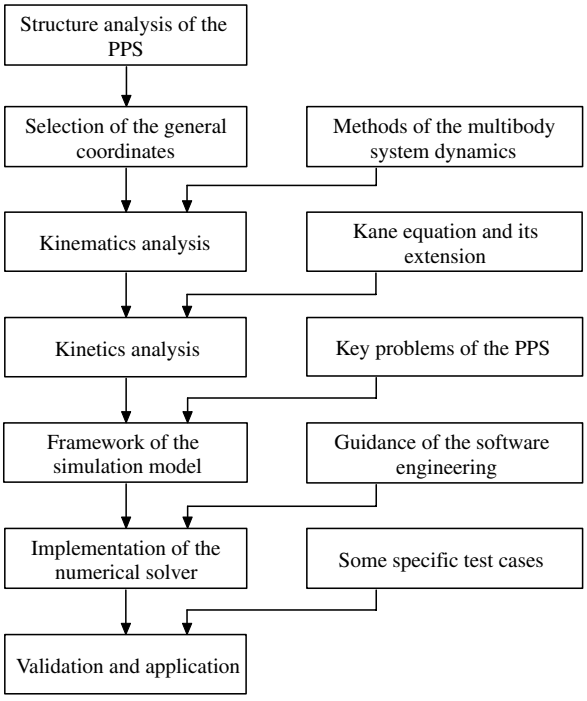

Fig. 1 Scheme of the algorithm framework.

II. Algorithm Framework

In this section, the details of the framework of our algorithm to simulate the PPS by considering the parachute systems as a special multibody system will be introduced. Our algorithm includes the following aspects (Fig. 1).

1) Analyze the kinematics of the PPS based on the methods of multibody system dynamics following its structural analysis and selection of general coordinates. The vector of generalized coordinates (VGC), vector degrees of freedom (VDOF), and map matrices will be introduced in this part.

2) Study the kinetics by using the Kane equation and its extension for the variable-mass system.

3) Build the framework of the simulation model after considering some key problems of the PPS, such as parachute deployment, parachute cluster, and sling system.

4) Implement the numerical solver according to the model framework and the software engineering.

5) Illustrate the algorithm with several examples.

A. Assumptions

The following assumptions were used in the present study.

1) During the airdrop process, the forces acting on the system include the gravity and aerodynamics forces.

2) Distortion of the shape of the parachute canopies was negligible after full inflation. The parachute was an axisymmetric rigid canopy with elastic suspension lines.

3) The aerodynamic forces generated by suspension lines were negligible.

4) The forces resulting from twisted risers and bridles were neglected.

B. Model of the PPS

As shown in Fig. 2, the PPS type is different for various application situations. However, all PPS are essentially identical from a multibody dynamics viewpoint. Specifically, each PPS, as a free multibody system during airdrop, is composed of four components with different features (Table 1).

These four parts were processed differently in this paper. The fully inflated parachute was regarded as a semirigid body composed of a rigid canopy connected to elastic suspension lines, because parachutes are the major parts of PPS. Furthermore, the interaction forces between the semirigid parachute and its connected bodies were considered. A similar approach was adopted to describe the inflating parachute, introducing the drag coefficient and the drag area, which are changing during the inflation process. For the purpose of snatch-force analysis, the canopy was treated as a mass point, as the lines were stretched out because it remained packed in the deployment bag. The confluence fittings were considered as point masses, and the suspension lines were considered as elastic constraints. According to assumption 4, only exerted forces were acted by these lines without torques. Finally, the payload was simulated as a simple rigid body.

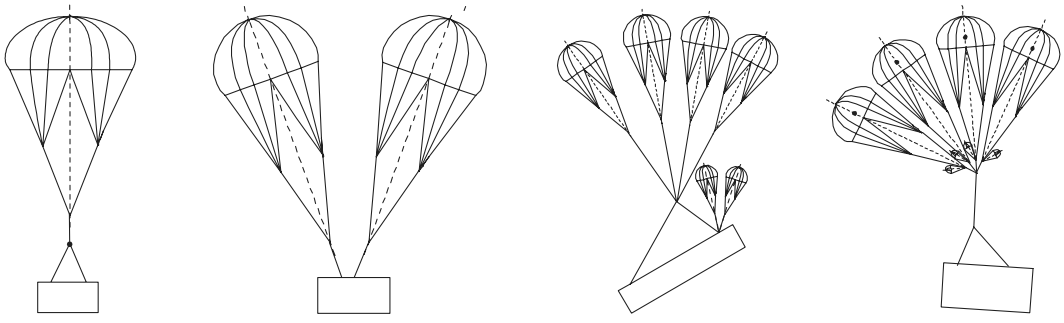

Fig. 2 Schematic for different parachute-payload systems.

Table 1 Dynamics features of four components included in PPS

Item	Mass	Inertia	Apparent mass	Mass variable	Aerodynamic force	Elastic	DOF
Parachute	✓	✓	✓	✓	✓	✓	3
Payload	✓	✓	×	×	✓	×	6
Line	×	×	×	×	×	✓	N/A
Confluence fitting	✓	×	×	×	×	×	3

[a]The symbol ✓ means it is necessary to be considered, and the symbol × means it is unnecessary to be considered.

System structural analysis is the first step to model a multibody system. The virtual body was introduced as a basic unit to build the topology of the PPS and represent the kinematic parameters of rigid bodies in this study. As translation and rotation movements each involve 3 DOF, each virtual body in this algorithm is allowed to move in no more than 3 DOF to unify the representation of the equation of motion with matrices and vectors of the third order. In the case in which a rigid body has more than 3 DOF, it must be represented by two virtual bodies. As demonstrated in Fig. 3a, two parachutes are connected to the payload by a riser (AB) and two bridles (BC1 and BC2). The corresponding topology is depicted in Fig. 3b. Two things should be noted: first, the payload with the center point $O1$ was decomposed into two virtual bodies to represent its translational (first virtual body) and rotational parameters (second virtual body). Next, two bridles were considered as constraints. This treatment is different from that in previous research.

The VDOF is defined as a combination of three possible DOF of each virtual body to make expressions of equation of motion more concise. Similarly, if a real body has 6 DOF, it must be expressed by two VDOF, whereas most of them need only one VDOF.

C. Vector of Generalized Coordinates

According to the definition of VDOF, the VGC was defined to indicate the VDOF. The VGC consisted of three generalized coordinates: $\boldsymbol{q} = (q_1\ q_2\ q_3)^T$. There are only two types of VGC used in this model, and they are well suited for the parachute systems containing axisymmetrical objects and lines. One kind of VGC is based on the cable axes coordinates $\boldsymbol{q} = (\gamma, d, \vartheta)^T$ and another is developed in light of the Euler angle triplet $\boldsymbol{q} = (\gamma, \varphi, \vartheta)^T$. The processes to form both types are shown in Fig. 4.

Using VGC, we can obtain the linear and angular velocity vector for VGC with respect to each virtual body's local frame by two transform matrices $\boldsymbol{H}^{\Omega}$ and $\boldsymbol{H}^{h}$ (as listed in Table 2): $\boldsymbol{\omega}_c = \boldsymbol{H}^{\Omega}\dot{\boldsymbol{q}}$ and $\boldsymbol{v}_c = \boldsymbol{H}^{h}\dot{\boldsymbol{q}}$.

For more generalized conditions, the matrices are slightly different if the virtual body has less than 3 DOF. For example, if d is fixed by the constraint in the VGC of $\boldsymbol{q} = (\gamma, d, \vartheta)^T$, the $\boldsymbol{H}^{h}$ will be zero. By using VGC, all of the derivations shown subsequently can be conducted in the form of vectors and matrices. The uniform equations using a matrix and vector array can then be formulated.

D. Kinematics Analysis

Generally, a real system consisting of m rigid bodies can be represented by n virtual bodies. The vector arrays of linear and angular velocity for the real system and the virtual-body system in the global frame are defined as $\boldsymbol{V} = (\boldsymbol{V}_1\ \ \boldsymbol{V}_2\ \ \cdots\ \ \boldsymbol{V}_m)^T$, $\Omega = (\Omega_1\ \ \Omega_2\ \ \cdots\ \ \Omega_m)^T$, $\boldsymbol{v} = (\boldsymbol{v}_1\ \ \boldsymbol{v}_2\ \ \cdots\ \ \boldsymbol{v}_n)^T$, $\boldsymbol{\omega} = (\boldsymbol{\omega}_1\ \ \boldsymbol{\omega}_2\ \ \cdots\ \ \boldsymbol{\omega}_n)^T$. In addition, $\boldsymbol{q} = (\boldsymbol{q}_1\ \ \boldsymbol{q}_2\ \ \cdots\ \ \boldsymbol{q}_n)^T$ and $\dot{\boldsymbol{q}} = (\dot{\boldsymbol{q}}_1\ \ \dot{\boldsymbol{q}}_2\ \ \cdots\ \ \dot{\boldsymbol{q}}_n)^T$ are defined to denote the vector of the generalized coordinates and their derivative for the virtual-body system, respectively,

The matrix form of kinematic equations could thus be derived through the topology analysis of the virtual-body system (see [1] for details regarding the detailed derivation process):

$$\boldsymbol{\omega} = \boldsymbol{\beta}\dot{\boldsymbol{q}} \tag{1}$$

$$\dot{\boldsymbol{\omega}} = \boldsymbol{\beta}\ddot{\boldsymbol{q}} + \boldsymbol{\sigma} \tag{2}$$

$$\boldsymbol{v} = \boldsymbol{\alpha}\dot{\boldsymbol{q}} \tag{3}$$

$$\dot{\boldsymbol{v}} = \boldsymbol{\alpha}\ddot{\boldsymbol{q}} + \boldsymbol{\eta} \tag{4}$$

where $\boldsymbol{\beta}$, $\boldsymbol{\alpha}_1$, $\boldsymbol{\alpha}_0$, and $\boldsymbol{\alpha}$ indicate the matrices with matrices as elements; $\boldsymbol{\sigma}$, $\boldsymbol{\eta}$, and $\boldsymbol{\alpha}_2$ represent the vectors composed of vectors; $\boldsymbol{\beta}_{ij} = -\boldsymbol{C}_j^{\Omega}\boldsymbol{T}_{ji}$, $\boldsymbol{\sigma} = -\boldsymbol{T}^T\boldsymbol{D}^{\Omega}$, $\boldsymbol{\alpha}_{0,ij} = -\boldsymbol{C}_j\boldsymbol{T}_{ji}$, $\boldsymbol{\alpha}_{1,ij} = -\boldsymbol{D}_j\boldsymbol{T}_{ji}$, $\boldsymbol{\alpha} = \boldsymbol{\alpha}_0 + \boldsymbol{\alpha}_1\boldsymbol{\beta}$, $\boldsymbol{\eta} = \boldsymbol{\alpha}_1\boldsymbol{\sigma} - \boldsymbol{T}^T\boldsymbol{E}^{\Omega}$, $\boldsymbol{C}_i^{\Omega} = \boldsymbol{H}_{0,i}\boldsymbol{H}_i^{\Omega}$, $\boldsymbol{D}_i^{\Omega} = [\boldsymbol{H}_{0,i}\dot{\boldsymbol{H}}_i^{\Omega} + \boldsymbol{S}(\boldsymbol{\omega}_i)\boldsymbol{C}_i^{\Omega}]\dot{\boldsymbol{q}}_i$, $\boldsymbol{C}_i = \boldsymbol{H}_{0,i}\boldsymbol{H}_i^{h}$, $\boldsymbol{D}_i = -\boldsymbol{S}(\boldsymbol{H}_{0,i}\boldsymbol{d}_i)$, and $\boldsymbol{E}_i = \boldsymbol{S}(\boldsymbol{\omega}_i)(2\boldsymbol{C}_i\dot{\boldsymbol{q}}_i + \boldsymbol{D}_i\boldsymbol{\omega}_i)$.

To get the kinematics parameters of real bodies from those of corresponding virtual bodies, we introduced the map matrices $\boldsymbol{H}_{b,h}^{\Omega}$ and $\boldsymbol{H}_{b,h}^{H}$ and defined $\boldsymbol{\Omega} = \boldsymbol{H}_{b,h}^{\Omega}\boldsymbol{\omega}$ and $\boldsymbol{V} = \boldsymbol{H}_{b,h}^{H}\boldsymbol{v}$. Then the partial velocity and partial angular velocity of the ith real body to the jth VGC are determined as $\dot{\boldsymbol{\Omega}}_{i,j}' = \partial\boldsymbol{\Omega}_i/\partial\dot{\boldsymbol{q}}_j$ and $\dot{\boldsymbol{V}}_{i,j}' = \partial\boldsymbol{V}_i/\partial\dot{\boldsymbol{q}}_j$, respectively. Using the map matrix, matrices of the partial velocities $\dot{\boldsymbol{V}}'$ and the partial angular velocities $\dot{\boldsymbol{\Omega}}'$ of the real-body system can be linked by $\dot{\boldsymbol{V}} = \boldsymbol{H}_{b,h}^{h}\boldsymbol{\alpha}$ and $\dot{\boldsymbol{\Omega}}' = \boldsymbol{H}_{b,h}^{\Omega}\boldsymbol{\beta}$.

E. Kinetics Analysis

For a PPS consisting of m real bodies, the vector arrays of the external force $\boldsymbol{F}^o$ and torque $\boldsymbol{M}^o$ are defined as $\boldsymbol{F}^o = (\boldsymbol{F}_1^o\ \ \boldsymbol{F}_2^o\ \ \cdots\ \ \boldsymbol{F}_m^o)^T$ and $\boldsymbol{M}^o = (\boldsymbol{M}_1^o\ \ \boldsymbol{M}_2^o\ \ \cdots\ \ \boldsymbol{M}_m^o)^T$. Both the force and torque are the resultant of the aerodynamic force,

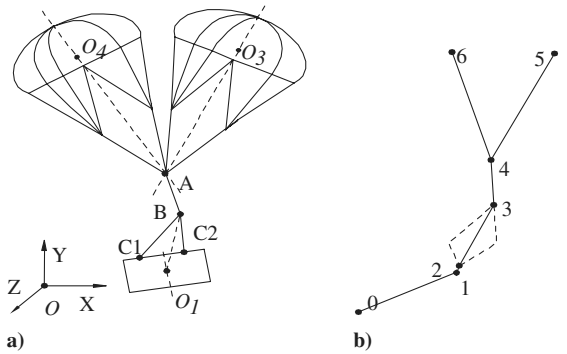

a) b)

Fig. 3 Configuration and topology of a sample system.

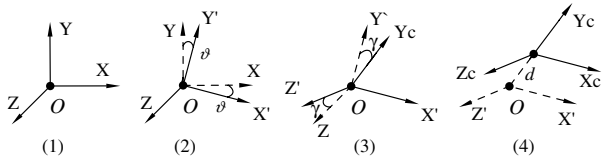

a) VGC based on the cable axes coordinate

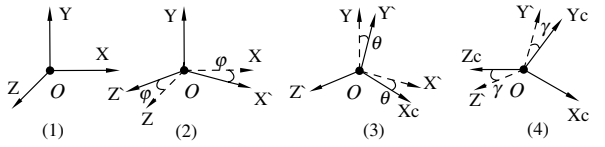

b) VGC based on the Euler angle triplet

Fig. 4 Process to create the VGC.

Table 2 Transform matrices of VGC

VGC	$\boldsymbol{H}^{\Omega}$	$\boldsymbol{H}^{h}$
$\boldsymbol{q} = (\gamma, d, \vartheta)^T$	$\begin{pmatrix} 1 & 0 & 0 \\ 0 & 0 & \sin\gamma \\ 0 & 0 & \cos\gamma \end{pmatrix}$	$\begin{pmatrix} 0 & 0 & 0 \\ 0 & 1 & 0 \\ 0 & 0 & 0 \end{pmatrix}$
$\boldsymbol{q} = (\gamma, \varphi, \vartheta)^T$	$\begin{pmatrix} 1 & \sin\vartheta & 0 \\ 0 & \cos\vartheta\cos\gamma & \sin\gamma \\ 0 & -\cos\vartheta\sin\gamma & \cos\gamma \end{pmatrix}$	$\begin{pmatrix} 0 & 0 & 0 \\ 0 & 0 & 0 \\ 0 & 0 & 0 \end{pmatrix}$

gravity, and contributing interaction forces (discussed subsequently). The aerodynamic force and torque are the most important forces applied on the PPS and can be computed according to the kinematic parameters and aerodynamic coefficients obtained from experiment or numerical simulation. Similarly, the vector array of the generalized active $\boldsymbol{F}$ for the entire system is defined as $\boldsymbol{F} = (\boldsymbol{F}_1 \quad \boldsymbol{F}_2 \quad \cdots \quad \boldsymbol{F}_n)^T$. The generalized force for the jth body ($j = 1, \ldots, n$), $\boldsymbol{F}_j$, can be deduced as follows:

$$\boldsymbol{F}_j^T = \sum_{i=1}^{m} (\boldsymbol{F}_i^{oT} \dot{\boldsymbol{V}}'_{i,j} + \boldsymbol{M}_i^{oT} \dot{\boldsymbol{\Omega}}'_{i,j}) \tag{5}$$

Thus, the vector array of generalized active force $\boldsymbol{F}$ is

$$\boldsymbol{F} = (\boldsymbol{H}_{b,h}^{H} \boldsymbol{\alpha}')^T \boldsymbol{F}^o + (\boldsymbol{H}_{b,h}^{\Omega} \boldsymbol{\beta}')^T \boldsymbol{M}^o \tag{6}$$

where $\boldsymbol{\alpha}'_{i,j} = \boldsymbol{\alpha}_{i,j}^T$, $\boldsymbol{\beta}'_{i,j} = \boldsymbol{\beta}_{i,j}^T$, and $i,j = 1, \ldots, m$.

As with the generalized active force, the vector arrays of the inertia force $\boldsymbol{F}^a$ and torque $\boldsymbol{M}^a$ are defined as $\boldsymbol{F}^a = (\boldsymbol{F}_1^a \quad \boldsymbol{F}_2^a \quad \cdots \quad \boldsymbol{F}_m^a)^T$ and $\boldsymbol{M}^a = (\boldsymbol{M}_1^a \quad \boldsymbol{M}_2^a \quad \cdots \quad \boldsymbol{M}_m^a)^T$ for the whole system. They can be formulated in accordance with the inertia force and torque for each body:

$$\boldsymbol{F}^a = -\boldsymbol{m} \boldsymbol{H}_{b,h}^{H} (\boldsymbol{\alpha} \ddot{\boldsymbol{q}} + \boldsymbol{\eta}) \tag{7}$$

$$\boldsymbol{M}^a = -\boldsymbol{J} \boldsymbol{H}_{b,h}^{\Omega} (\boldsymbol{\beta} \ddot{\boldsymbol{q}} + \boldsymbol{\sigma}) - \boldsymbol{M}^b \tag{8}$$

where $\boldsymbol{M}^b = \boldsymbol{\omega}_i \times (\boldsymbol{J}_i \boldsymbol{\omega}_i)$, and $\boldsymbol{m}$ represents the mass matrix, which is a diagonal matrix and each element is also the mass matrix of $\boldsymbol{m}_i$, where each rigid body $i = 1, \ldots, m$. It should be noted that the additional mass matrix must be taken into account for the parachute.

Based on the preceding equations, the matrix-form generalized inertia force $\boldsymbol{F}^* = (\boldsymbol{F}_1^* \quad \boldsymbol{F}_2^* \quad \cdots \quad \boldsymbol{F}_n^*)^T$ can be expressed as follows:

$$\boldsymbol{F}^* = -\boldsymbol{\lambda} \ddot{\boldsymbol{q}} - (\boldsymbol{H}_{b,h}^{H} \boldsymbol{\alpha}')^T \boldsymbol{m} \boldsymbol{H}_{b,h}^{H} \boldsymbol{\eta} + (\boldsymbol{H}_{b,h}^{\Omega} \boldsymbol{\beta}')^T (\boldsymbol{J} \boldsymbol{H}_{b,h}^{\Omega} \boldsymbol{\sigma} + \boldsymbol{M}^b) \tag{9}$$

where

$$\boldsymbol{\lambda} = (\boldsymbol{H}_{b,h}^{H} \boldsymbol{\alpha}')^T \boldsymbol{m} \boldsymbol{H}_{b,h}^{H} \boldsymbol{\alpha} + (\boldsymbol{H}_{b,h}^{\Omega} \boldsymbol{\beta}')^T \boldsymbol{J} \boldsymbol{H}_{b,h}^{\Omega} \boldsymbol{\beta} \tag{10}$$

It is obvious that $\boldsymbol{\lambda}$ is a positive definite matrix.

Finally, the simplest equation of motion for this system can be formulated by using the Kane equation $\boldsymbol{F} + \boldsymbol{F}^* = \boldsymbol{0}$:

$$\boldsymbol{\lambda} \ddot{\boldsymbol{q}} = \boldsymbol{\mu} \tag{11}$$

$$\boldsymbol{\mu} = (\boldsymbol{H}_{b,h}^{H} \boldsymbol{\alpha}')(\boldsymbol{F}^o - \boldsymbol{m} \boldsymbol{H}_{b,h}^{H} \boldsymbol{\eta}) + (\boldsymbol{H}_{b,h}^{\Omega} \boldsymbol{\beta}')(\boldsymbol{M}^o - \boldsymbol{J} \boldsymbol{H}_{b,h}^{\Omega} \boldsymbol{\sigma} - \boldsymbol{M}^b) \tag{12}$$

F. Interaction Forces Contributing to Generalized Active Force

The interaction forces stemming from elastic lines used in the parachute system, such as suspension lines, risers, and bridles, should be considered due to their contribution to the generalized active force. If the VGC for a specific elastic line is $\boldsymbol{q}_r = (\gamma_r \quad d_r \quad \vartheta_r)^T$, in line with the cable axes coordinate, the force $\boldsymbol{F}_r$ along this line can be written in the local frame bonded with the line as $\boldsymbol{F}_r = (0 \quad -f_r \quad 0)^T$, and

$$f_r = k_r (d_r - d_{r0}) + c_r \dot{d}_r \tag{13}$$

where k_r and c_r are the stiffness and damping coefficient, and d_{r0} represents the initial length of the line. The contribution of the elastic force to the generalized active force for the jth VGC is calculated as

$$\boldsymbol{F}_{rj}^T = \boldsymbol{F}_r^T \frac{\partial (\dot{\boldsymbol{q}}_r - \dot{\boldsymbol{q}}_{L(r)})}{\partial \dot{\boldsymbol{q}}_j} = \boldsymbol{F}_r^T \frac{\partial (\boldsymbol{C}_r \dot{\boldsymbol{q}}_r + \boldsymbol{D}_r \boldsymbol{\omega}_r)}{\partial \dot{\boldsymbol{q}}_j} \tag{14}$$

Depending on the relationship between indices, Eq. (14) can be expanded to the following form:

$$\boldsymbol{F}_{rj}^T = \begin{cases} \boldsymbol{F}_r^T (\boldsymbol{C}_r + \boldsymbol{D}_r \boldsymbol{C}_j^{\Omega}) & j = r \\ \boldsymbol{F}_r^T \boldsymbol{D}_r \boldsymbol{C}_j^{\Omega} & j \in L_r \\ 0 & \text{else} \end{cases} \tag{15}$$

Considering

$$\boldsymbol{F}_r^T \boldsymbol{D}_r \boldsymbol{C}_j^{\Omega} = 0 \tag{16}$$

and

$$\boldsymbol{C}_r^T \boldsymbol{F}_r = \boldsymbol{H}_r^{hT} \boldsymbol{H}_{0,r}^T \cdot \boldsymbol{H}_{0,r} \cdot (0 \quad -f_r \quad 0)^T = (0 \quad -f_r \quad 0)^T \tag{17}$$

we then derived $\boldsymbol{F}_{rj}$ in the local frame of the line:

$$\boldsymbol{F}_{rj} = \begin{cases} (0 \quad -f_r \quad 0)^T & j = r \\ (0 \quad 0 \quad 0)^T & j \neq r \end{cases} \tag{18}$$

III. Some Key Problems for the Parachute System

Before employing the algorithm to a real PPS, some specific simulation models need to be developed. The algorithm for the PPS includes the parachute opening model including the parachute and the payload as separated 6 DOF masses, the parachute cluster model in which each parachute has 6 DOF considering contact between parachute, and the slung-payload system model allowing for the slings and risers as elastic or inelastic constraints. These models, as the foundation to simulate a complex PPS, were integrated into the simulation using this algorithm.

A. Model of Parachute Opening

The parachute opening process can usually be divided into two subprocesses: deployment and inflation. The deployment process starts from the instant when the extraction parachute pulls the deployment bag away from the payload, which may remain attached to the aircraft. In this paper, it is assumed that the extraction parachute deploys the main parachute. Most often (though not always) the suspension lines will be pulled from the deployment bag first, then when the suspension lines are deployed and fully extended, the suspension lines will pull the parachute canopy from the deployment bag. The inflation process begins the instant the parachute first captures the air mass and reshapes it by interacting with the surrounding airflow, and it ends when the parachute is fully inflated. As a result of the rapid changes in the shape and drag of the canopy during inflation and the massive undetermined contributing factors that cannot be accurately predicted, it is difficult to model both subprocesses with a high degree of accuracy.

In this section, the dynamic model of the parachute opening process was built based on the framework described in previous sections and Ge and Cheng's [13] equation. Ge and Cheng extended Kane's equation aiming at the nonholonomic variable-mass system and introduced the generalized thrust to consider the effects of the variable mass. Computing the thrust is the key part for using Ge and Cheng's [13] equation to study a variable-mass system.

Considering the general system built previously, the thrust $\boldsymbol{F}_i^r$ for the ith body $\boldsymbol{B}_i$ with variable mass m_i, can be calculated as $\boldsymbol{F}_i^r = (0 \quad F_i^r \quad 0)^T$ in the local frame of body $\boldsymbol{B}_i$:

$$\boldsymbol{F}_i^r = \dot{m}_i \boldsymbol{u}_i \tag{19}$$

where $\boldsymbol{u}_i$ is the velocity difference between $\boldsymbol{B}_i$ and the part separated from it, and $\dot{m}_i$ denotes the time derivative of m_i.

Using Ge and Cheng's [13] equation, the generalized thrust for the jth VGC can be stated as

$$\boldsymbol{F}_j' = \sum_{i=1}^{Nv} \boldsymbol{F}_i^r \frac{\partial \dot{\boldsymbol{r}}_i}{\partial \dot{\boldsymbol{q}}_j}, \qquad j = 1 \sim N_v \tag{20}$$

where N_v is the index number of the body with variable mass.

Now we can apply Eqs. (19) and (20) to simulate the parachute opening process. The first step is to characterize the topology of the system during the opening process. The simplest configuration of the parachute opening is given in Fig. 5a, in which only one parachute and one payload were included. Figure 5b shows the corresponding topology. The payload is depicted as the first and second virtual bodies, and the parachute is modeled as the third virtual body. The opening direction is along the Y axis of the parachute.

The second step is to compute F^r, the magnitude of $\boldsymbol{F}^r$ for each variable-mass body. In the deployment process, the mass of the parachute is variable. We can calculate the magnitude by

$$F^r = \bar{m} u^2 \tag{21}$$

where $\bar{m}$ is the mass distribution of the parachute along the deployment direction, and u indicates the speed difference between the parachute and payload.

During the inflation process, the apparent mass of the parachute alters with the air flowing into and out of the canopy. Within the canopy, the airflow is extremely complicated. For the sake of simplification, the change in the additional mass $\dot{m}_f$ is considered as the only variation of the parachute mass. The difference of speed between the parachute and payload is computed as follows:

$$u = \dot{m}_f / (\rho A) \tag{22}$$

Hence, the thrust is

$$F^r = \dot{m} u = \dot{m}_f^2 / (\rho A) \tag{23}$$

B. Parachute Cluster Contact Model

Parachute cluster systems were developed to increase system reliability, to avoid using a single excessively large canopy (as the failure of a single canopy will not cause a system failure in a properly designed system), and to be manufactured and packed easily. The methods used to design a cluster parachute system were at first based on empirical data. In such studies, the cluster is treated as a single parachute by using a cluster coefficient to account for the lower drag of a canopy used in a cluster as compared with the drag of an individual canopy. As discovered in the test, the phenomena such as collision and lead lag indicate that one canopy may commonly inflate more quickly or slowly than others in real-world operation, especially under the complex flowfield. The angled orientation of the individual canopies and corresponding reduction in drag coefficient cannot be simulated by using traditional methods in which a cluster coefficient is required.

In contrast, the simulation model provided in Sec. II is capable of easily investigating this issue thoroughly by separately modeling each parachute canopy included in a cluster. The most important remaining problem is to model the contact between parachutes in cluster, which is very challenging with the current state of the art.

The penalty formulation, which is usually used to simulate the contact occurred in elastic solid, was applied to shaping the contact force between parachutes to simplify the simulation. Considering that the fully inflated parachute can still be treated as an elastic body despite its extreme flexibility, a similar formulation could be adopted for the parachute. Figure 6 exhibits the basic schematic for the contact between two parachutes that connect to point I. Parachute centers of gravity are J and K, respectively. In this figure, point C is the contact center point of the contact surface. The forces and torque acting on the parachute J are defined as $\boldsymbol{F}_c$ and $\boldsymbol{T}_c$, and $\boldsymbol{u}$ is the direction of collision.

In the model, the contact force defined in Eq. (24) was modeled as a spring. The contact force is thus the function of the deformation length δ and deformation speed $\dot{\delta}$ during the contact process [14]:

$$\boldsymbol{F}_c = (K\delta^n + D\dot{\delta})\boldsymbol{u} \tag{24}$$

where K, D, and n are the coefficients. All of these coefficients should be reconstructed from experiment data or numerical simulation based on the structure dynamics methods, such as a finite element method.

The torque can then be calculated according to the force:

$$\boldsymbol{T}_c = (\boldsymbol{r}_c - \boldsymbol{r}_j) \times \boldsymbol{F}_c \tag{25}$$

where $\boldsymbol{r}_c$ and $\boldsymbol{r}_j$ are the position vectors for points C and J.

After acquiring the force and torque, the easiest way to use them is to consider them as the external forces acting on each parachute. In addition, there is a better way to build the detailed system model with this algorithm.

The contribution of the contact force and torque to the generalized active force for the rth VGC can be rewritten:

$$\boldsymbol{F}_r^c = \boldsymbol{F}_c \left(\frac{\partial \dot{\boldsymbol{r}}_j}{\partial \dot{\boldsymbol{q}}_r} - \frac{\partial \dot{\boldsymbol{r}}_k}{\partial \dot{\boldsymbol{q}}_r} \right) + \boldsymbol{T}_c \left(\frac{\partial \boldsymbol{\omega}_j}{\partial \dot{\boldsymbol{q}}_r} - \frac{\partial \boldsymbol{\omega}_k}{\partial \dot{\boldsymbol{q}}_r} \right) \tag{26}$$

Combined with $L^1(J) = L^1(K) = I$, $\dot{\boldsymbol{r}}_j = \boldsymbol{C}_j \dot{\boldsymbol{q}}_j + \boldsymbol{D}_j \boldsymbol{\omega}_{L(j)}$, and $\dot{\boldsymbol{r}}_k = \boldsymbol{C}_k \dot{\boldsymbol{q}}_k + \boldsymbol{D}_k \boldsymbol{\omega}_{L(k)}$, Eq. (26) can be expanded to different form depending upon the value of r:

$$\boldsymbol{F}_r^c = \begin{cases} \boldsymbol{F}_c \boldsymbol{C}_j + \boldsymbol{T}_c \boldsymbol{C}_j^{\Omega} & r = j \\ -\boldsymbol{F}_c \boldsymbol{C}_k - \boldsymbol{T}_c \boldsymbol{C}_k^{\Omega} & r = k \\ \boldsymbol{F}_c (\boldsymbol{D}_j - \boldsymbol{D}_k) \boldsymbol{C}_j^{\Omega} & r \in L_i \\ 0 & \text{else} \end{cases}$$

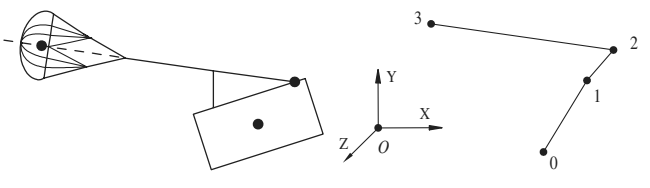

a) b)

Fig. 5 Configuration and topology for the parachute opening process.

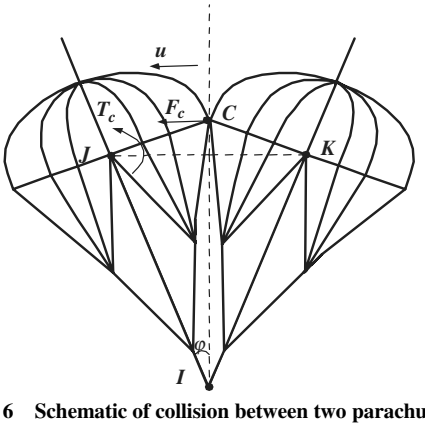

Fig. 6 Schematic of collision between two parachutes.

C. Model of the Sling System Considering the Elastic Bridles

The sling system is composed of individual slings, or bridles, and was treated as two rigid objects linked by many elastic-line constraints. A general scheme for analyzing elastic-bridle constraints is given in Fig. 7. O_i and O_j are the mass center of the two virtual bodies B_i and B_j, respectively. O_k indicates the confluence point, with the biggest index between the two branches from 0 to i and from 0 to j. DE connects B_i at the point of D and B_j at E. DE was modeled as a constraint.

To characterize the virtual body of DE, the VGC $\boldsymbol{q} = (\gamma_s \quad d_s \quad \vartheta_s)^T$ with respect to virtual body B_i was defined. Thus, DE can be treated as one contribution interaction force in this system.

The global position of DE can be derived by both the reference-frame transform matrix and the relative position:

$$\boldsymbol{r}_{\mathrm{DE}} = H_{0,i}H_{i,s}\tilde{\boldsymbol{r}}_{\mathrm{DE}} = \boldsymbol{r}_j + \boldsymbol{r}_{jE} - (\boldsymbol{r}_i + \boldsymbol{r}_{iD}) \tag{28}$$

Expanding Eq. (28) in a body reference frame, we obtained

$$\dot{\boldsymbol{r}}_{\mathrm{DE}} = \dot{\boldsymbol{r}}_j + \dot{\boldsymbol{r}}_{jE} - (\dot{\boldsymbol{r}}_i + \dot{\boldsymbol{r}}_{iD}) \tag{29}$$

$$\tilde{\dot{\boldsymbol{r}}}_{\mathrm{DE}} + \boldsymbol{\omega}_{\mathrm{DE}} \times \boldsymbol{r}_{\mathrm{DE}} = \dot{\boldsymbol{r}}_{iji} + \tilde{\dot{\boldsymbol{r}}}_{jE} + \boldsymbol{\omega}_{jE} \times \boldsymbol{r}_{jE} - \tilde{\dot{\boldsymbol{r}}}_{iD} - \boldsymbol{\omega}_{iD} \times \boldsymbol{r}_{iD} \tag{30}$$

Finally,

$$\boldsymbol{H}_s\dot{\boldsymbol{q}}_s = \sum_{t\geq k, t\in L_j} \boldsymbol{H}_t\dot{\boldsymbol{q}}_t - \sum_{l\geq k, l\in L_i} \boldsymbol{H}_l\dot{\boldsymbol{q}}_l - S(\boldsymbol{H}_{0,j}\boldsymbol{r}_{jE})\boldsymbol{\omega}_j + S(\boldsymbol{H}_{0,i}\boldsymbol{r}_{iD})\boldsymbol{\omega}_i \tag{31}$$

where $\boldsymbol{H}_z = \boldsymbol{C}_z + \boldsymbol{D}_z\boldsymbol{C}_z^{\Omega}$. Therefore, $\boldsymbol{q}_s$ and $\dot{\boldsymbol{q}}_s$ can be calculated by solving Eqs. (28) and (29), respectively.

IV. Implementation of the Solver

Guided by the software engineering rules, a numerical solver for the algorithm was developed by using C++. The solver is able to read the configuration files of a rigid parachute-payload system, including the properties of mass, structure, and aerodynamics of each component in the real system; the topology information of the virtual-body system, such as the linkage and constraint relationship; the information of the wind field; and the settings of the simulation.

Overall, the initial step to use the proposed algorithm to conduct a specific simulation is to analyze the real parachute system and build a representative topology. The main area that needs special consideration is the simulation of the parachute system operation over the entire process, from the drop through full inflation of the parachute system to achieving stable descent. Although the topology behavior changed with the deployment of each parachute, a script file is used to create the connection during each stage after the stage identification in our solver. The stage here means the duration when the system topology remained invariable.

V. Results and Validation

To testify our algorithm, three examples were simulated. The first one is a simple computation of the motion of a mass point compared with the results from the commercial software Adams, the second is the simulation of the Mars lander mission with the comparison with [5], and the third is a more complex simulation of the HCADS compared with the tests. All simulations are performed by using a fourth-order Runge–Kutta method with 0.0001 s as the step length.

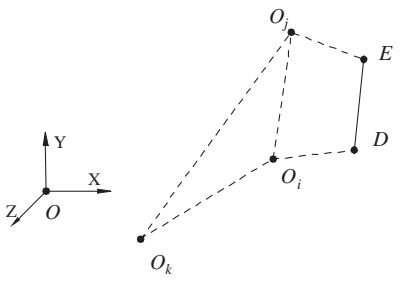

Fig. 7 Analysis of the elastic bridle.

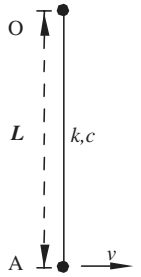

Fig. 8 Case configuration.

A. Motion of a Mass Point

The motion of a single mass point A moving around a fixed center point O through an elastic line was analyzed. The configuration and initial values of the system are listed in Fig. 8 and Table 3. To compare the performance of the algorithm described in this study and that of commercial software, simulations were conducted using the algorithm and Adams, respectively. The trajectory comparison of point A under different initial velocities v is given in Fig. 9. It should be noted that the results of the simulation using the algorithm agree well with those yielded from Adams, which is a general multibody dynamics simulation software validated by massive examples. It is worthwhile to point out that the algorithm in this study is more suitable than Adams for the parachute system simulation. The reason is that our algorithm is better suited to deal with the special issues of the parachute, such as parachute opening, intercanopy contact, and computation of the aerodynamic force of the parachute and payload.

B. Mars Lander Mission

The results calculated using the algorithm proposed in this study were compared with those obtained from [5], in which the simulations were performed by using POST and MATLAB under different condition for the PPS employed in the Mars lander mission. The detailed configuration of the PPS can be found in [5].

The first case for the purpose of validation was that the system was dropped vertically with no initial velocity, with the vertical riser having 1_cm of slack, and the condition was given in Fig. 3a shown in [5]. As depicted in Fig. 10, our simulation results confirmed the results from [5], except for the initial phase (from 1.4 to 2.0 s). This difference may result from the different models used to describe the parachute. Specifically, the parachute was considered as a flexible body in this model, whereas it was simulated as a rigid body in [5].

The next case was the parachute opening, which was obtained from Figs. 15 and 16 of [5]. This case begins when the parachute is ejected from the back of the entry capsule and lasts for 3.0 s. A very similar parachute inflation profile was generated (Fig. 11). The forces acting on the parachute calculated by this model were compared with those of [5] and are demonstrated in Fig. 12.

Table 3 Value of the parameters

Body	Parameter	Value	Unit
Line	Length L	10.00	m
Line	Elastic coefficient k	4500.00	N/m
Line	Dumping coefficient c	45.00	N/(m/s)
Point	Mass	10.00	kg

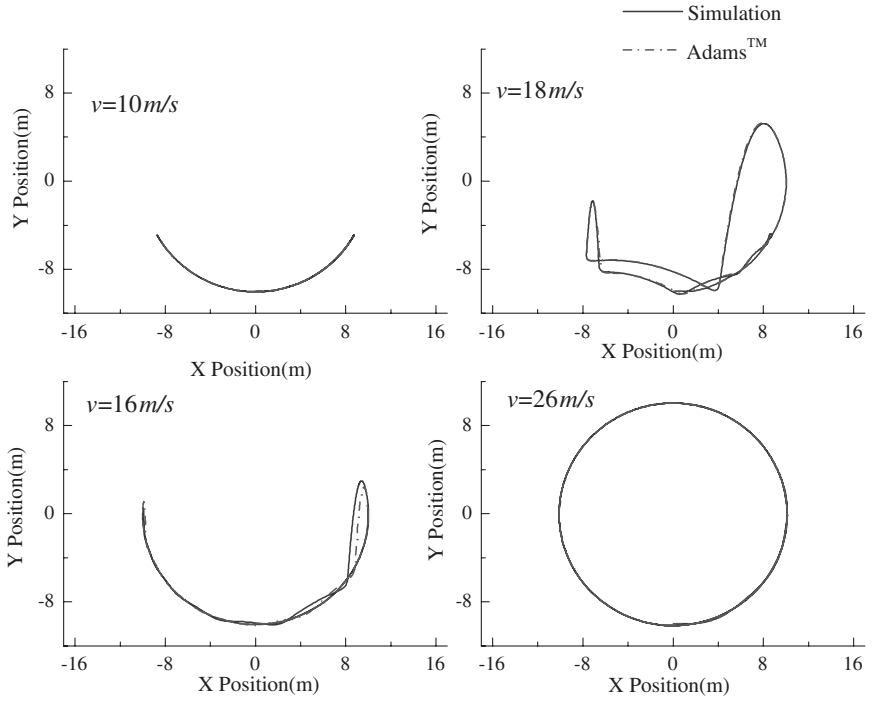

Fig. 9 Trajectories of the moving mass point.

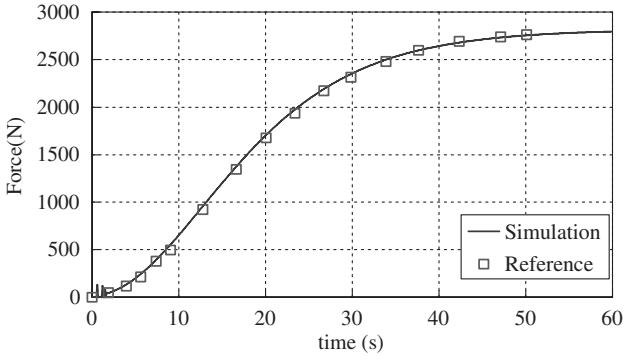

Fig. 10 Net line force on the parachute (our simulation vs [3]).

The first stage started from the time the cargo was extracted until the sling bridles were stretched. During this period, the pilot parachute deployed and subsequently lifted the deployment bags containing the main parachutes away from the payload, and then the riser and a pair of sling bridles were snatched orderly. The real system and the topology are described in Figs. 13a and 13b, respectively, in which the cargo is depicted as the first and second virtual bodies and the third–fifth virtual bodies are the deployment bags, the confluence fitting, and the pilot parachute.

The next stage starts from the time the main parachute deployment bag opens and ends when the payload lands. First, four drogues and a main suspension line will deploy. Then the main parachutes deploy and inflate. Within this duration the payload experienced a large oscillation. The real system and corresponding topology graphs are displayed in Figs. 14a and 14b, respectively. The four main parachutes are treated as four single bodies (fifth–eighth virtual

C. Typical HCADS

A more complex simulation was conducted for a typical HCADS, which consisted of 10 parachutes and a payload weight of greater than 7 t. More details about the HCADS can be found in [1]. The entire deployment and inflation process after the cargo was extracted from the airplane was too complicated to be simulated easily without dividing the total process into several shorter stages and considering them separately. Therefore, a two-stage dividing method was employed in this study.

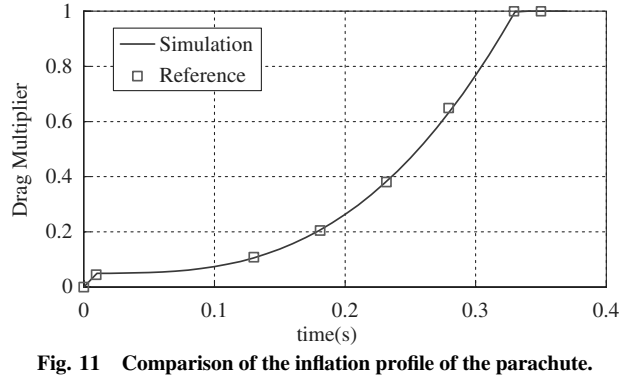

Fig. 11 Comparison of the inflation profile of the parachute.

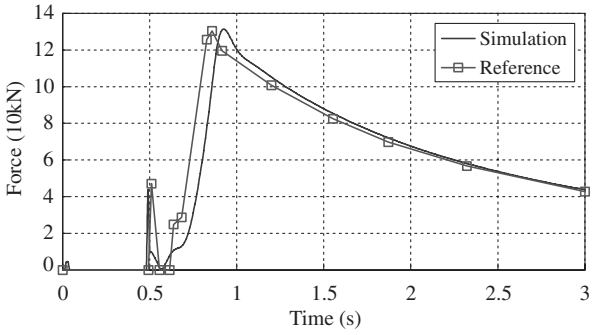

Fig. 12 Comparison of the force acted on the parachute.

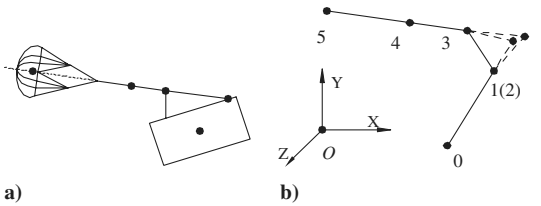

Fig. 13 Configuration of the first stage.

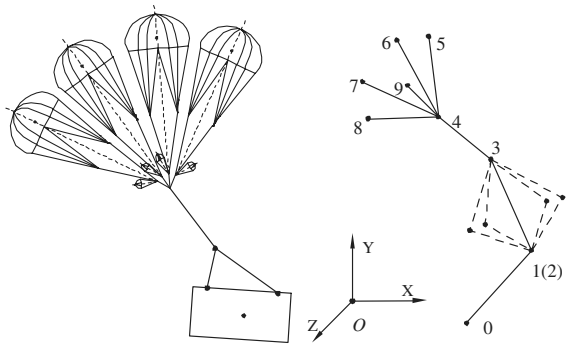

Fig. 14 Configuration of the second stage.

bodies) and the four drogue parachutes are considered as a single body (ninth virtual body) in Fig. 14b, because the total drag force of the drogues is less than 5% of that of the main parachute cluster. Additionally, the cargo is depicted as the first and second virtual bodies, and the third and fourth virtual bodies are the confluence fitting and the confluence point of the main parachutes.

The airdrop tests for a typical HCADS were conducted by an Il-76 aircraft flying at a nominal altitude about 600 m above ground level and with a nominal airspeed of 320–380 km/h. The simulations were conducted according to the test condition, and the trajectories of the mass center of each component and the attitude of the cargo are shown in Figs. 15–17. The coefficients in Eq. (24) required to achieve the simulation were reconstructed from the test data. The simulated trajectories of the mass center of the four main chutes were identical before inflation, because they were close together during deployment and then separated and diverged after inflation. The oscillation of the cargo around the Z axis is large at first, but dampens out, and the platform becomes stable. But the rotation around the Y axis is not attenuated or damped, which was observed in the tests as well.

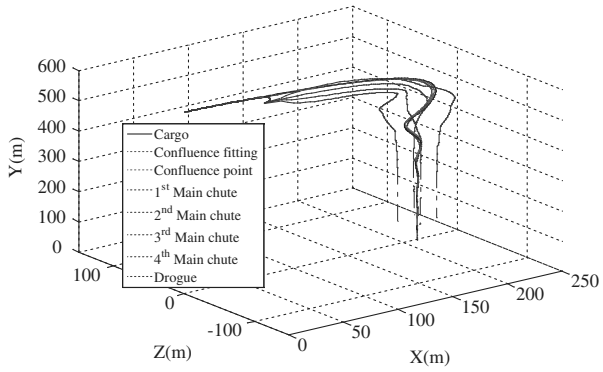

Fig. 15 Trajectories of the mass center of each component.

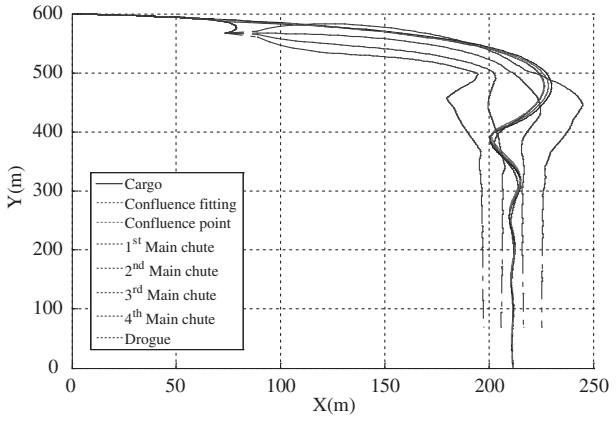

Fig. 16 Trajectories of the mass center of each component (side view).

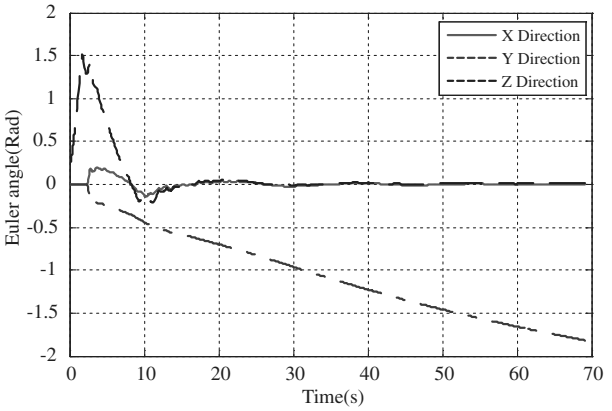

Fig. 17 Attitude of the cargo.

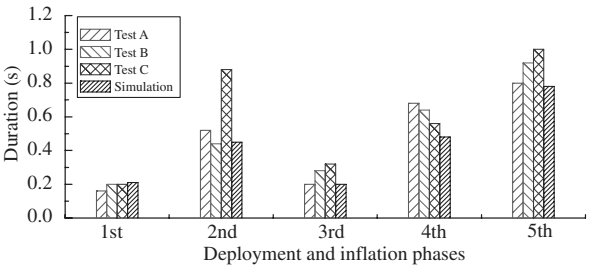

Fig. 18 Comparison of the duration time of each parachute deployment.

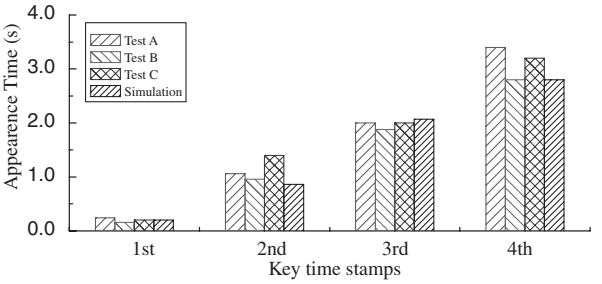

Fig. 19 Comparison of key time in airdrop process.

The duration of the deployment and inflation process of each parachute is given in Fig. 18, in which the first to fourth phases are the deployment and inflation times of the pilot and drogue, respectively, and the fifth is the deployment time of the main parachute.

Figure 19 shows the instant of the key time stamps appearing in the airdrop process after the cargo cleared the ramp of the aircraft floor. In this figure, the stamps represented the instants when the pilot parachute stretched and inflated as well as when the main parachutes began to deploy and stretched. As shown by these two graphs, the simulation results were just in the range of the fluctuation of the three sets of test data.

Although the validation of the algorithm described in this paper is still ongoing, the preceding results give confidence that this algorithm could be a useful and universal tool to predict and simulate many types of parachute-payload systems.

VI. Conclusions

A novel algorithm based on the dynamics of a multibody system and Kane equation to simulate the parachute systems was presented and validated. This model can be used not only for preflight predictions but also for parachute system design. The model has been successfully used for a range of simulations to analyze various

parachute systems, including the heavy-cargo airdrop system, the Shenzhou spacecraft recovery system, a paratrooper system, and an airdrop system of a manned cabin. However, the model needs further validation and verification. This will be our future direction. In addition, there were some conditions in which the point masses may be very small compared with the payload because of the point-mass assumption used to simplify the confluence point. Such an assumption may result in numerical stiffness during the solving process. To overcome these flaws, a smaller calculation step length or implicit methods may be required to keep the stability of the integration progress. It is affordable and acceptable in the offline simulation of such parachute systems.

Acknowledgments

The authors wish to thank financial support from the Foundation of Aeronautics Science of China (no. 04E51046) and Feng Yang and John Watkins for their helpful suggestions.

References

[1] Yang, C. X., and Ke, P., "Development and Validation of the Multi-Body Simulation Software for the Heavy Cargo Airdrop System," AIAA Paper 2007-2572, May 2007.

[2] Fallon, E. J., "Parachute Dynamics and Stability Analysis of the Queen Match Recovery System," AIAA Paper 91-0879, Apr. 1991.

[3] Moulin, J., "Recovery System Simulation: Link Modelization," AIAA Paper 93-1249, May 1993.

[4] Raiszadeh, B., and Queen, E. M., "Mars Exploration Rover Terminal Descent Mission Modeling and Simulation," *14th AAS/AIAA Space Flight Mechanics Meeting*, AIAA, Reston, VA, Feb. 2004, pp. 2661–2676.

[5] Raiszadeh, B., and Queen, E. M., "Partial Validation of Multibody Program to Optimize Simulated Trajectories II (POST II) Parachute Simulation with Interacting Forces," NASA TM-2002-211634, Apr. 2002.

[6] Cuthbert, P. A., "A Software Simulation of Cargo Drop Tests," AIAA Paper 2003-2132, May 2003.

[7] Cuthbert, P. A., and Desabrais J., "Validation of a Cargo Airdrop Software Simulator," AIAA Paper 2003-2133, May 2003.

[8] Cuthbert, P. A., and Conley, G. L., "A Desktop Application to Simulate Cargo Drop Tests," AIAA Paper 2005-1623, May 2005.

[9] Potvin, J., Charles, R., and Desabrais K., "Comparative DSSA Study of Payload-Container Dynamics before, During and After Parachute Inflation," AIAA Paper 2007-2564, May 2007.

[10] Raiszadeh, B., "Multibody Parachute Flight Simulations for Planetary Entry Trajectories Using 'Equilibrium Points,'" 13th AAS/AIAA Space Flight Mechanics Meeting, AIAA, Reston, VA, Feb. 2003, pp. 903–914.

[11] Balaram, J., Austin, R., Banerjee, P., Bentley, T., Henriquez, D., Martin, B., et al., "DSENDS—A High-Fidelity Dynamics and Spacecraft Simulator for Entry, Descent and Surface Landing," IEEE 2002 Aerospace Conference, Inst. of Electrical and Electronics Engineers, Piscataway, NJ, Mar. 2002, pp. 3343–3359. doi:10.1109/AERO.2002.1035313

[12] Eberhard, P., and Schiehlen, W., "Computational Dynamics of Multibody Systems: History, Formalisms, and Applications," *Journal of Computational and Nonlinear Dynamics*, Vol. 1, Jan. 2006, pp. 3–12. doi:10.1115/1.1961875

[13] Ge, Z. M., andCheng, Y. H., "Extended Kane's Equations for Non-Holonomic Variable Mass System," *Journal of Applied Mechanics*, Vol. 49, No. 2, June 1982, pp. 429–431.

[14] Lankarani, H. M., and Nikravesh, P. E., "Continuous Contact Force Models for Impact Analysis in Multibody System," *Nonlinear Dynamics*, Vol. 5, No. 2, Mar. 1994, pp. 193–207.